Article

Reducibility Studies of Ceria, $Ce_{0.85}Zr_{0.15}O_2$ (CZ) and Au/CZ Catalysts after Alkali Ion Doping: Impact on Activity in Oxidation of NO and CO

Ewa Maria Iwanek (nee Wilczkowska) [1,*], Leonarda Francesca Liotta [2,*], Shazam Williams [3], Linjie Hu [3], Huitian Ju [3], Giuseppe Pantaleo [2], Zbigniew Kaszkur [4], Donald W. Kirk [5], Wojciech Patkowski [1] and Marek Gliński [1]

1   Faculty of Chemistry, Warsaw University of Technology, 00-664 Warsaw, Poland; wpatkowski@ch.pw.edu.pl (W.P.); marek.glinski@pw.edu.pl (M.G.)
2   Istituto per lo Studio di Materiali Nanostrutturati (ISMN)-CNR, I-90146 Palermo, Italy; giuseppe-pantaleo@cnr.it
3   DCL International Inc., Concord, ON L4K 4T5, Canada; swilliams@dcl-inc.com (S.W.); rhu@dcl-inc.com (L.H.); jju@dcl-inc.com (H.J.)
4   Institute of Physical Chemistry, Polish Academy of Sciences, 01-224 Warsaw, Poland; zkaszkur@ichf.edu.pl
5   Department of Chemical Engineering and Applied Chemistry, University of Toronto, Toronto, ON M5S 3E5, Canada; don.kirk@utoronto.ca
*   Correspondence: ewa.iwanek@pw.edu.pl (E.M.I.); leonardafrancesca.liotta@cnr.it (L.F.L.)

Abstract: The aim of these studies was to perform thorough research on the influence of alkali metal ions (Li, Na, K and Cs) on the properties of nanogold catalysts supported on ceria–zirconia. The addition of alkali metal ions onto CeO_2 further affected the reducibility, which was not noted for the Zr-doped support ($Ce_{0.85}Zr_{0.15}O_2$). Despite the substantial impact of alkali metal ions on the reducibility of ceria, the activity in CO oxidation did not change much. In contrast, they do not have a large effect on the reducibility of Au/CZ but suppressed the activity of this system in CO oxidation. The results show that for CO oxidation, the negative effect of potassium ions is greater than that of sodium, which corresponds to the shift in the T_{max} of the reduction peak towards higher temperatures. The negative effect of Li^+ and Cs^+ spans 50% CO conversion. The negative effect was visible for CO oxidation in both the model stream and the complex stream, which also contained hydrocarbons and NO. In the case of NO oxidation to NO_2, two temperature regimes were observed for Au + 0.3 at% K/CZ, namely in the temperature range below 350 °C; the effect of potassium ions was beneficial for NO oxidation, whereas at higher temperatures, the undoped gold catalyst produced more NO_2.

Keywords: reducibility; ceria; cerium-zirconium mixed oxide; Au catalysts; CO oxidation; alkali metal ions

1. Introduction

With the regulation of NO emissions, the maximum allowable limit of this gas in vehicle exhaust streams has been constantly decreased by institutions in Europe (Euro 6 standards) and North America (Environmental Protection Agency and Environment and Climate Change Canada standards). Studies of NO oxidation have been reported for catalysts, such as supported catalysts: both noble metals and metal oxides, as well as other types of systems [1–5]. It is noteworthy that carbonaceous materials can be used both as catalyst supports, as well as the active phase [6]. According to the literature, the amount of NO_2 formed depends not only on the catalyst properties but also on the partial pressure of oxygen in the feed and that of the product, which has been shown to inhibit NO oxidation in some cases. In studies performed on perovskite-type oxide, it was concluded that doping $SrFeO_{3-\delta}$ with Co and Mn ions influences parameters such as oxygen release/storage

profiles, oxygen migration barrier and conditions of phase transformation, which, in turn, affect the activity of the obtained system in low-temperature NO oxidation [4]. Some studies have shown that the presence of alkali metal ions affects the adsorption of NO on char [7]. The results of density functional theory (DFT) modelling show that with the addition of Li, Na or K onto the surface of char, the energy released on NO adsorption increases compared to that on an undoped surface, and the effect is the most pronounced for potassium [7].

In the case of carbon monoxide, the current aim is pushing the temperature of its conversion to lower values by proper catalyst design. Gold is known for its high activity in low-temperature CO oxidation [8–11]. Catalysts studied for this reaction are very frequently supported on ceria [2–16], although other oxides have also been tested as supports [17]. An unsupported cobalt oxide catalyst has also shown to achieve very high conversions of CO at low temperatures [18]. In a paper that employed a variety of different cobalt precursors, such as cobalt nitrate, cobalt acetate, cobalt carbonate and cobalt oxalate, substantially different results in CO oxidation were noted for the obtained cobalt catalyst, with a T_{50} span of more than 50 °C [18]. Among the research on ceria-based low-temperature CO oxidation catalysts is a study on the effect of doping the support with Fe, La and Zr on the activity of the catalyst [16], which showed that the best effect is observed when ceria contains zirconia. An interaction of the active phase with the support can sometimes be observed when considering the C 3d region in X-ray photoelectron spectroscopy (XPS) spectra and profiles in temperature-programmed reduction (TPR) studies, as in the case of Ag-CeZrO$_2$ and Au-Ag/CeZrO$_2$ catalysts [19]. Moreover, in the case of palladium catalysts for low-temperature CO oxidation, it has been shown that the active sites are formed thanks to the interaction of Pd with CeO$_2$ [15]. It has also been shown that Ru interacts with the ceria surface, and the proper amount of the active phase leads to the formation of oxygen vacancies, which makes the catalyst more active [20]. It was therefore our goal to perform a thorough investigation of how the presence of alkali ions influences the reducibility of supports and the gold catalyst and hence its activity in CO oxidation.

Alkali metal ions have been shown to have a beneficial effect on activity in soot oxidation [21–24], as well as the reduction of coking of catalysts [25,26]. Recent studies have shown that the presence of potassium ions results in a detrimental effect on the activity of gold catalysts. This topic has not been well investigated; no other alkali ions have been used to dope these systems, and the effect of alkali metal ion loading has not been studied thus far. In this paper, we aim to fill this gap. In the case of soot oxidation, studies in which potassium carbonate was deposited onto silica, which is not active in soot oxidation by itself, have shown that the resultant activity of the obtained systems could only be attributed to potassium ions [21]. The decomposition of the carbonate species to an oxide does not lead to deactivation of potassium ions. Furthermore, the results of the authors' investigation on the activity of potassium ions deposited onto CeO$_2$, ZrO$_2$ and MgO showed a correlation between the Sanderson electronegativity of the support and the activity of the lattice oxygen of the support [21]. However, the three oxides differ substantially in terms of their crystal structure. Zirconia can exhibit one of three structures (monoclinic, tetragonal or cubic), MgO crystallizes in the NaCl-type cubic structure and CeO$_2$ has a fluorite-type structure, which means that a comparison of ceria alone and ceria doped with a small amount of zirconium ions, which retains its fluorite-type structure, may be an interesting next step. Previous studies have shown that when approximately 15at.% of cerium ions are substituted with zirconium ions, i.e., $n_{Zr}/(n_{Ce}+n_{Zr}) = 0.15$, there is only one phase present, namely the fluorite-type ceria structure. Such a solid solution is commonly applied in exhaust systems. One of the aims of the studies presented in this paper was to investigate the effect of the presence of alkali metal cations on the reducibility of ceria obtained by different methods and on that of ceria–zirconia.

2. Results

Before the reducibility of nanogold catalysts supported on ceria-based supports was determined, the reducibility of the supports themselves was tested. In this part of the study, two parameters were investigated, namely the influence of the method of synthesis and the addition of zirconium (coprecipitation). Two samples were synthesized from ammonium ceric nitrate: precipitated ceria (C_P), which is ceria synthesized by dissolving the precursor, precipitation of cerium hydroxide and calcination at 550 °C, as well as ceria obtained via thermal decomposition of ammonium ceric nitrate (C_{TD}), which was prepared by heating the precursor to 550 °C, causing a complete decomposition of the precursor. The results obtained from these two samples were compared to those of commercial ceria (C_C). Figure 1a–c depicts the morphology of these supports, as seen in scanning electron microscopy (SEM) images. It can be seen that the textural properties of the three samples significantly differ. Precipitated ceria (Figure 1a) has substantially large particles, which appear to be compact chunks, i.e., no porosity is seen in the image. In contrast, the other two ceria samples (Figure 1b, sample via thermal decomposition and Figure 1c, commercial ceria) appear to be composed of nanoaggregates. In the image of C_{TD}, spherical particles can be observed, which are typical of solids obtained from molten salts, as well as wispy features, which are a sign of recrystallization. In the image of the commercial ceria, signs of pronounced sintering can be observed, which is indicative of a high-temperature treatment of the powder. Coprecipitated ceria–zirconia (Figure 1d) appears very similar to the precipitated ceria.
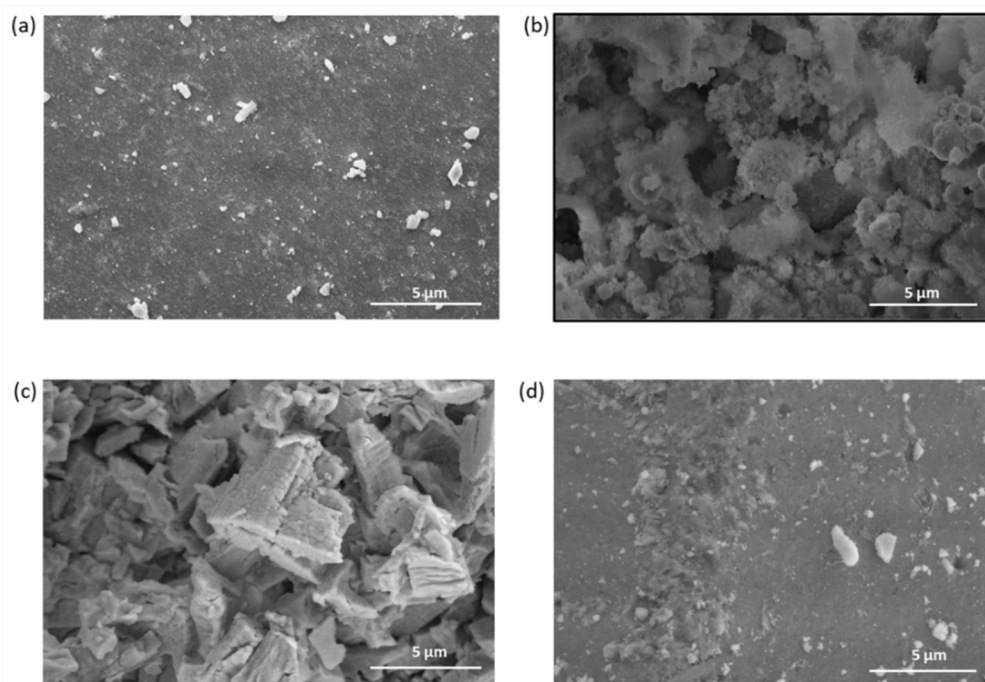

Figure 1. SEM images of ceria and ceria–zirconia: (**a**) ceria obtained via precipitation, (**b**) ceria obtained via thermal decomposition, (**c**) commercial ceria and (**d**) ceria–zirconia at a magnification of 20,000 times.

The results derived from characterization studies, for example, of nitrogen physisorption, x-ray diffraction (XRD) and temperature-programmed reduction are reported in Table 1. The specific surface area of commercial ceria is very low, i.e., 5.7 m^2/g, likely due to the preparation conditions or high-temperature treatment of this sample. The surface area values of C_P and C_{TD} are 46 and 18 m$^2 \cdot$ g^{-1}, respectively (Table 1). It is therefore odd that with the highest surface area of all three samples, the SEM image of C_P does not exhibit visible porosity. The answer to this question can be found in the mean average

pore size for this sample, which is less than 3 nm and therefore below the detection limit of the instrument used. Commercial ceria, although it exhibits a very low surface area, has pores with a mean size of slightly more than 33 nm, so they can be seen in the SEM image (Figure 1c). In the case of C_{TD}, the mean pore size is more than 15 nm; therefore, pores can also be distinguished in the picture. The cerium–zirconium mixed oxide, which was obtained by coprecipitation, has a higher surface area than the precipitated ceria, showing the well-known increase in temperature resistance upon the addition of zirconium. Nevertheless, its mean pore size is very similar to that noted for C_P (Table 1).

Table 1. Results of characterization measurements: lattice parameter of the support (a), average support particle size (D), specific surface area (S_{BET}), mean pore size and degree of reduction of ceria in the supports. The absolute error of the determination is written in brackets after the number.

Measurement	Parameter	Sample			
		C_C	C_P	C_{TD}	$CeZrO_2$
N_2 physisorption	S_{BET} [$m^2 \cdot g^{-1}$]	5.7 (2)	46 (4)	18 (3)	75 (4)
	Mean pore diameter [nm]	33.1 (1)	2.9 (1)	15.4 (1)	2.6 (1)
XRD	a [Å]	data	5.408 (2)	5.410 (2)	5.374 (2)
	D * [nm]	70 (5)	6.0 (4)	2.5 (3)	4.4 (3)
TPR	% Ce^{4+} to Ce^{3+} reduction	36 (2)	30 (2)	55 (2)	38 (2)

* The average particle size was calculated using the Scherrer equation.

The XPS results (Supplementary Information: Figure S1) show that the supports do not contain any impurities (Figure S1a) on their surface, and the Ce 3d detailed regions indicate that all four of the studied supports have the same oxidation state of ceria, i.e., the spectrum is typical of pure CeO_2, with no pronounced contribution from Ce^{3+} (Supplementary Information: Figure S1b). The Ce 3d regions were fitted with two sets of five components, as described in Materials and Methods. Examples depicting the fitted curves for C 1s, O 1s and Ce 3d of precipitated ceria are compiled in Figure S2. X-Ray Diffraction studies (Figure 2) confirmed that all four supports contain only one phase, namely the fluorite structure, ID 810792. It can be seen that the peak width at $\frac{1}{2}$ max of the signals of the commercial ceria is much smaller than that of the other samples. This is indicative of larger crystal domains, which could be due to a high-temperature treatment of the commercial ceria. The fitting of the signals in the diffraction patterns of ceria and cerium–zirconium mixed oxide shows the presence of the same type of structure in both (Figure 2b,c) but with an expansion of the unit cell and hence a larger lattice constant in the latter (Table 1) due to the incorporation of zirconium ions into the lattice. The particle size of the oxide is 6.0 nm for the ceria obtained via precipitation, 2.5 nm for the sample obtained via thermal decomposition and about 70 nm for the commercial ceria (Table 1). For the cerium–zirconium mixed oxide, the particle size is approx. 5 nm, as reported in [11].

In order to compare the surface groups found on the three types of ceria supports, attenuated total reflection Fourier transform infrared spectroscopy (ATR-FTIR) measurements were carried out, and the spectra were compared to those of the ceria precursor, ammonium ceric nitrate (Figure 3a top curve) and potassium carbonate used to prepare the solution for dosing of the supports (Figure 3a, bottom curve). Figure 3b–d each contain three spectra. The black curves correspond to the unmodified supports. It can be observed that the deposition of potassium carbonate on the surface of all three ceria samples leads to the formation of a bond that is not present in the spectrum of the potassium carbonate, i.e., the band at 1625 cm^{-1}. The appearance of this bond may be attributed to the interaction of the potassium carbonate with the support. The compilation shows a significant difference between the commercial ceria and the other two types of ceria. The spectrum of the commercial ceria does not contain visible signals from functional groups on the surface of this support. This is most likely the result of a very small surface area of this support (Table 1). The other two supports have very similar spectra, which contain peaks at

approximately 1625 cm^{-1}, 1510 cm^{-1} and 1315 cm^{-1}, all of which are ascribed to carbonate groups (mono and bidentate). It is noteworthy that with the addition of 0.3 at% potassium ions, none of the spectra changes substantially. However, samples with 3.0 at% potassium ions show an impact of the deposition on the relative quantity of functional groups present on the surface of the samples. In the case of commercial ceria (Figure 3b), the most intensive band in this spectrum is at 1365 cm^{-1}, which is also present in the spectrum of the potassium carbonate. The band at 1625 cm^{-1} is relatively larger for this sample than in the spectra of the other supports with 3.0 at% potassium ions (Figure 3c,d).
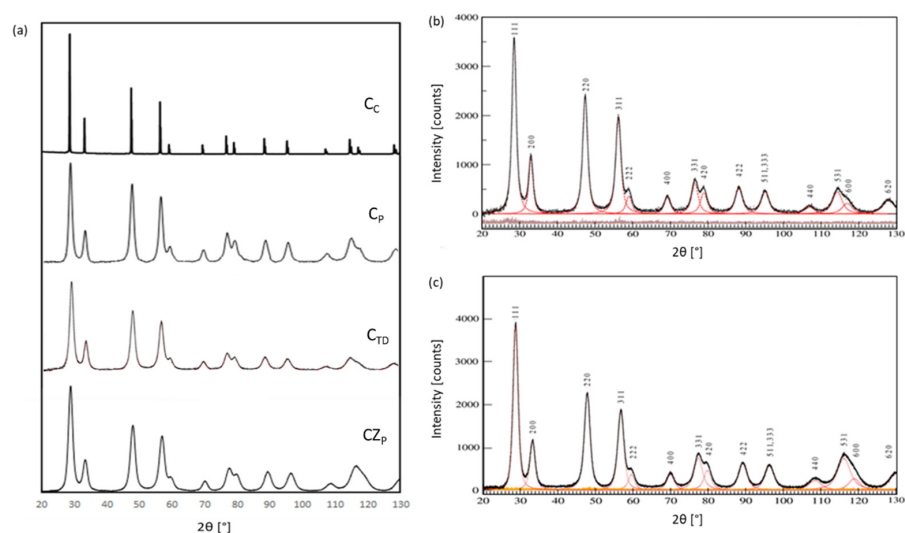

Figure 2. XRD patterns (**a**) of the three types of ceria supports and the cerium–zirconium mixed oxide and with fitted peaks for (**b**) ceria and (**c**) ceria–zirconia.
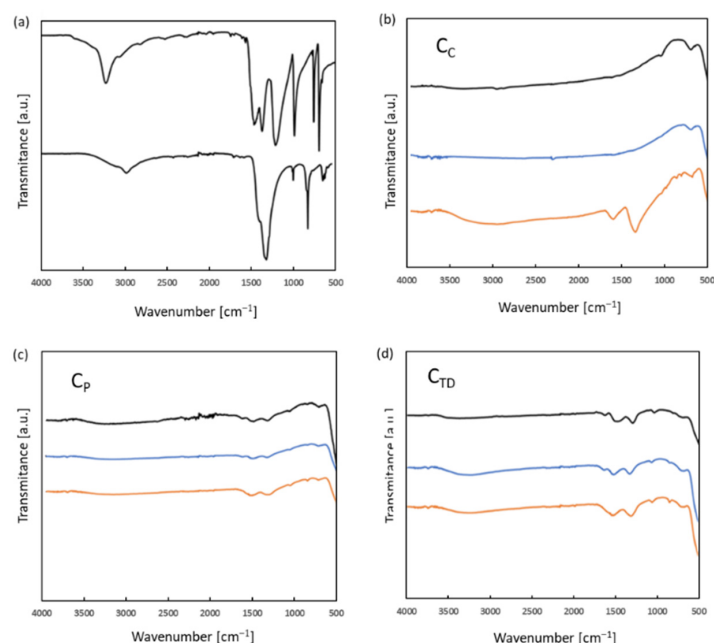

Figure 3. ATR-FTIR curves of (**a**) ammonium ceric nitrate (**top**) and potassium carbonate (**bottom**), as well as the three types of ceria supports, (**b**) C$_C$, (**c**) C$_P$ and (**d**) C$_{TD}$, without potassium (black curves) and with 0.3 at% (blue curves) and 3.0 at% (orange curves) potassium carbonate solution.

The TPR curves of the three types of ceria and that of the cerium–zirconium mixed oxide are depicted in Figure 4a. Each sample gives a different result, according to the fact that preparation conditions and textural properties may strongly affect the reduction profiles. The curve that corresponds to the precipitated ceria support has two reduction maxima: the first occurs at 453 °C and is assigned to the surface reduction, whereas the other one at 867 °C is due to the bulk reduction [27,28]. The commercial ceria has a pronounced reduction maximum at 880 °C and a very tiny maximum at 502 °C. This is in line with the small surface area of the sample and the large crystallite size. Among the ceria samples, the TD ceria, characterized by a relatively large surface area (but not the largest), showed a pronounced reduction maximum at 434 °C, with a shoulder at 517 °C. Then, the reduction of the bulk occurs at 854 °C. The low-temperature, two-peak shape could be a consequence of diffusional resistance associated within surface oxygen or could be due to the presence of surface CO_2, which desorbs when TPR perturbs the TCD signal [27]. The extent of reduction of cerium from Ce^{4+} to Ce^{3+} was calculated (Table 1) as 30% for commercial ceria, 36% for precipitated ceria and 55% for the thermally decomposed ceria. This value was approximately 38% for the precipitated cerium–zirconium mixed oxide.
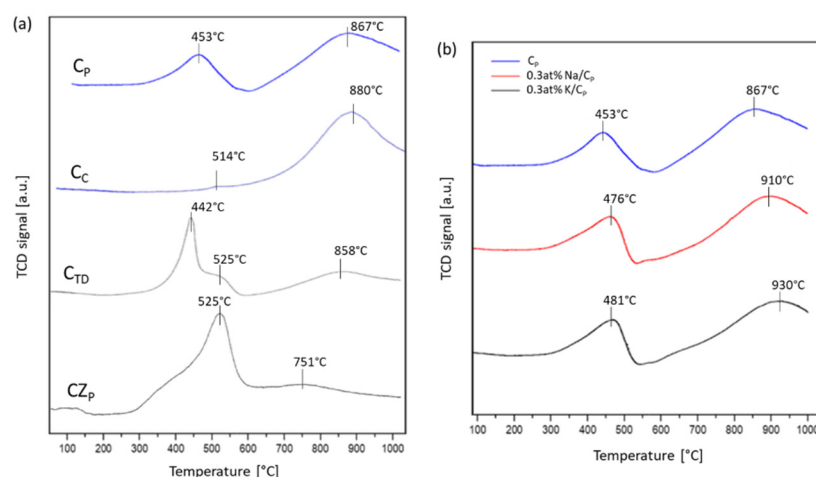

Figure 4. Temperature-programmed reduction profiles of (**a**) all three types of ceria and the cerium–zirconium mixed oxide and (**b**) precipitated ceria support after K^+ or Na^+ ion deposition.

It can be seen that the profile obtained for the cerium–zirconium mixed oxide is substantially different than that of the three types of ceria (Figure 4a) in that the reduction occurs mostly below 600 °C, and there is no reduction peak above 900 °C. The TPR curve of the ceria–zirconia solid solution had one major hydrogen consumption signal in a wide temperature range, i.e., 270–630 °C, and a small maximum at 770 °C, as previously reported [11], and is the same after the deposition of 0.3 at% potassium [11].

The TPR curves of precipitated ceria after deposition of sodium or potassium exhibit two distinct steps of hydrogen consumption, as in the case of the untreated sample, although the presence of the alkali metal cations results in a slight change of the shape of the TPR curve (Figure 4b). Both cations shift each of the maxima towards higher temperatures. The temperatures of the maxima are presented in Table 2. The first peak is shifted by 23 K and 28 K, whereas the second peak is shifted by 43 K and 63 K by sodium and potassium, respectively. The total volume of hydrogen consumed is the same (within experimental error) for all three samples, but the distribution between the two maxima might be slightly affected by the presence of alkali ions. This is a sharp contrast to our previous study of $Ce_{0.85}Zr_{0.15}O_2$, for which no difference was observed in the TPR profile upon the addition of potassium ions [11].

Table 2. TPR results: reduction temperatures and volumes determined for the precipitated ceria doped with potassium and sodium ions. The error of determination is written in brackets after the number.

Sample Parameter	Ceria	0.3% Na/Ceria	0.3 at% K/Ceria
T max 1 [°C]	453	476	481
Max. 1 volume [mL·g^{-1}]	6.2(4)	6.6(4)	7.2(5)
T max 2 [°C]	867	910	930
Max. 2 volume [mL·g^{-1}]	19.0(4)	18.7(4)	18.2(4)
Total volume [mL·g^{-1}]	25.2	25.3	25.4

The activity of the ceria samples in CO oxidation in the model stream was determined. The results are shown in Figure 5a, in which the CO conversion curves and temperatures of 50% conversion (T$_{50}$) are displayed. It can be seen that there is a very large discrepancy between their activity. All of them are inactive in CO oxidation below 200 °C. At 500 °C, the activity of the precipitated ceria is slightly more than 20%. The conversion of CO over the commercial ceria is 60%, whereas it is close to 100% for the ceria obtained from thermal decomposition. This is interesting, considering the shape of the obtained TPR curves (Figure 4) and the determined surface areas (Table 1). If the high activity of C$_{TD}$ is attributed to the fact that the majority of the reduction is finished below 500 °C, then it is difficult to understand the superiority of the activity of C$_C$ over C$_P$. Moreover, increased activity does not correlate with increased surface area. As previously mentioned, the commercial ceria has a substantially lower surface area than the precipitated sample, yet its activity in the model stream is higher. The three types of ceria behave very differently, despite having the same composition (elemental composition and phase composition).
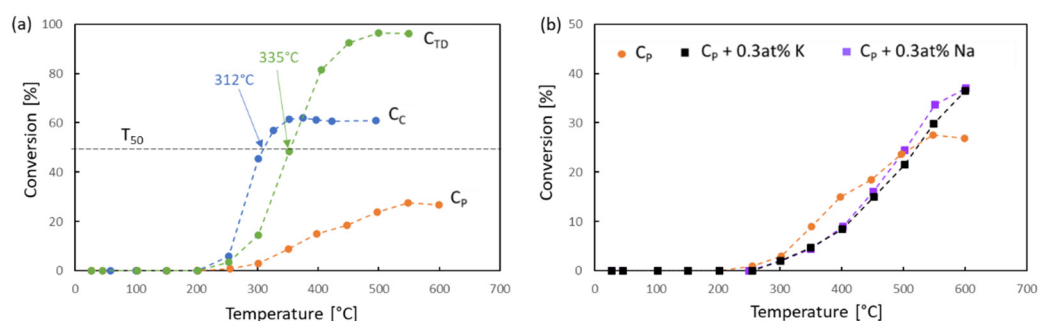

Figure 5. Activity of (**a**) different ceria supports in CO oxidation in the model stream, as well as (**b**) Na$^+$- and K$^+$-doped precipitated ceria.

The effect of doping the precipitated ceria support with 0.3 at% potassium and sodium ions on its activity in CO oxidation in the model stream is shown in Figure 5b. The precipitated ceria doped with potassium and sodium carbonate achieved a similar CO conversion to that of the undoped precipitated ceria. However, there seem to be two different regions. In the range of 250–500 °C, both the alkali-doped supports have a lower CO conversion, and above that temperature, the same two samples exhibit a higher activity than the undoped ceria. If the levelling off of the curve for the undoped support is due to coke formation, then the increased activity of the alkali-doped samples may be attributed to their activity in combustion of carbonaceous deposits and increasing the surface of ceria, which participates in CO oxidation.

The three TPR curves of the Au/CZ, Au + K/CZ and Au + Na/CZ samples confirm what our previous studies have shown about the influence of potassium ions on the reducibility of the gold catalyst and show that sodium also shifts the reduction temperature to a slightly higher value (Figure 6a). The conversion of CO in the model stream shows that the influence of the alkali metal ions is especially pronounced at lower temperatures

(Figure 6b). The order of activity is Au/CZ > Au0.3 at% Na/CZ > Au0.3 at% K/CZ, which is in line with the TPR data, as well as with the influence of these ions on the precipitated ceria support. Studies of alkali-doped Co_3O_4 as a low-temperature catalyst for CO oxidation also revealed a reduced activity for sodium and a further reduction of potassium [29]. It is the reverse order of their influence on their activity in soot oxidation [21] because in that reaction, oxide ions need to be stabilized on the surface to react with carbon, whereas in CO oxidation, they should be mobile rather than stabilized.
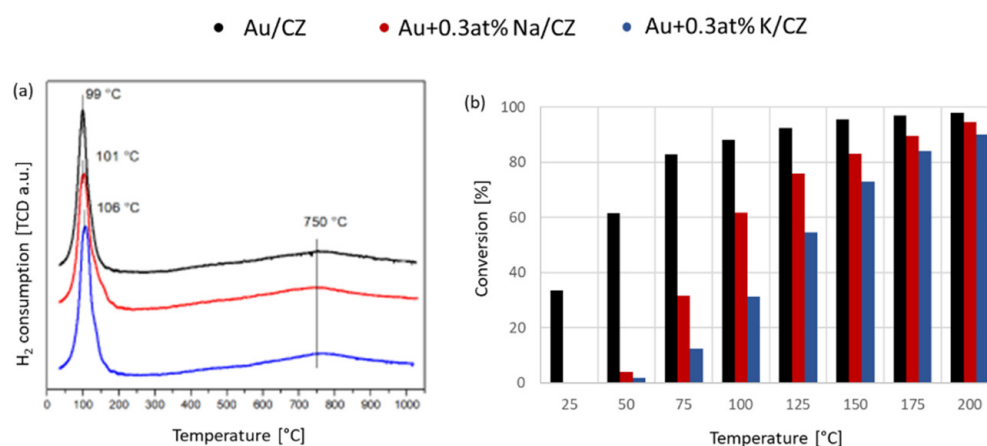

Figure 6. TPR curves (**a**) and CO oxidation activity (**b**) of Au/CZ, Au + 0.3 at% Na/CZ and Au + 0.3 at% K/CZ.

The TPR profiles of the same cerium–zirconium mixed oxide doped with 0.3 at% lithium, sodium, potassium and caesium ions are presented in Figure 7a. It can be seen that the curves are very similar and do not exhibit any pronounced differences. All of them have a low temperature reduction peak with a maximum at 539 °C and a much broader, higher-temperature reduction peak with a maximum at approximately 740 °C. However, when comparing the TPR profiles of the support doped with 0.3 and 3.0 at% K (Figure 7b), the shape changes, and the higher loading shifts the reduction temperature of the beginning of the reduction to higher values, although the maxima of neither reduction peaks are affected by the change of loading. The TPR profiles of the gold catalysts doped with 0.3 at% alkali cations all have the same shape and three reduction peaks with maxima at 144 °C, approximately 485 °C and 730 °C. A comparison of the gold catalysts with 0.3 and 3.0 at% alkali ions indicates that the loading does not change the reducibility of the lithium-doped catalyst. The shape of the TPR profiles of the other samples changes significantly upon the loading increase, and the first reduction peak is shifted to 255 °C for sodium, i.e., more than 100 K. It is shifted even further, to 267 °C, in the presence of 3.0 at% potassium ions. Both the T_{max} and the shape of the first reduction signal change (Figure 7c,d). It is noteworthy that the high-temperature shoulder visible in the profile of the catalyst doped with 3.0 at% sodium ions (Figure 7d grey curve) is more pronounced in the profile of the potassium-doped catalyst, and in the case of the caesium-doped sample, there are two maxima. The small middle signal merges with the first one. The third reduction signal is widened for catalysts with 3.0 at% Na, K and Cs but not for the Li-doped sample. This is due to the much lower mobility of lithium ions compared to that of the other alkali metal ions, which has been thoroughly studied in coal gasification [30].
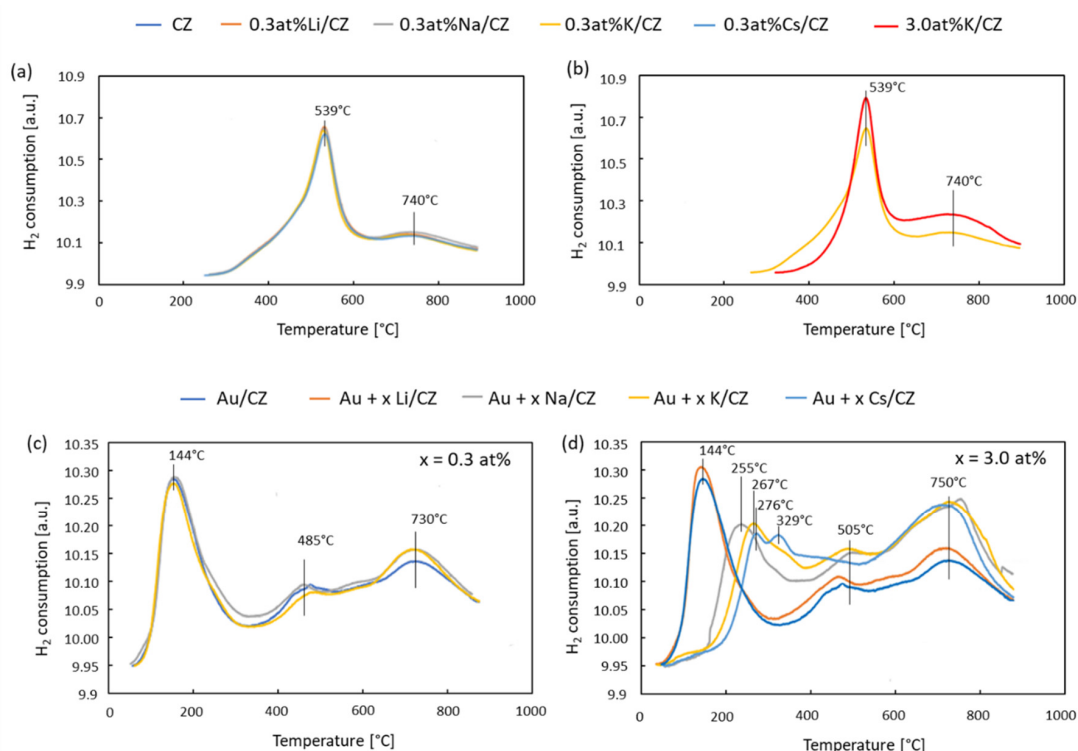
Figure 7. TPR profiles of (**a**) cerium–zirconium mixed oxide doped with 0.3 at% Li, Na, K and Cs ions, (**b**) comparison of 0.3 at% K/CZ and 3.0 at% K/CZ, (**c**) Au + 0.3 at% alkali metal ions/CZ and (**d**) Au + 3.0 at% alkali metal ions/CZ.

The SEM images of Au/CZ, Au + 0.3 at% Na/CZ and 0.3 at% Na/CZ are compiled in Figure 8, along with the energy-dispersive X-ray (EDX) maps showing the distribution of gold and sodium where applicable. The maps of the other elements present in the samples, namely oxygen, cerium and zirconium, are shown in Supplementary Information, Figure S3. It can be seen that these elements are distributed evenly on the surface of the samples. Furthermore, the distribution of gold is not changed by the addition of sodium (Figure 8a,b), although the predeposited gold influences the distribution of sodium (Figure 8b,c). The intensity of the sodium signal from the surface is stronger in the case of the gold catalyst. A similar observation was made with the other alkali metal ions deposited onto ceria–zirconia preloaded with gold and with the sequential deposition of gold and silver onto ceria–zirconia [19].

Studies in the complex stream, which, apart from CO, contains other components (for the detailed composition, see Materials and Methods), show that although the effect of potassium ions on the activity of a gold catalyst in CO oxidation is detrimental (Figure 9a), as reported by us earlier [11], its effect on the availability of oxygen for oxidation of NO is not correlated with the reducibility of the catalyst (Figure 9b). The amount of formed NO_2 in the post reaction mixture is greater for the Au + K/CZ catalyst than for Au/CZ for temperatures below 350 °C, which might be attributed to the effect of stabilization of NO on the surface by the potassium ions, as concluded from the DFT calculations of NO adsorption on carbon [7]. However, at higher temperatures, i.e., above 350 °C, the reverse is true, and the amount of NO_2 formed is greater on Au/CZ. This might suggest a change in the mechanism of NO oxidation above this temperature. A different mechanism for NO oxidation on chabazite zeolites was proposed in [31] and was explained as transition of the active sites. The NO_2 concentration in the outlet stream of the potassium-doped support is much higher than for Au + 0.3 at% K/CZ, which indicates a strong interaction of potassium ions with gold. In contrast, no such change is visible in the levels of unconverted CO (Figure 9a).
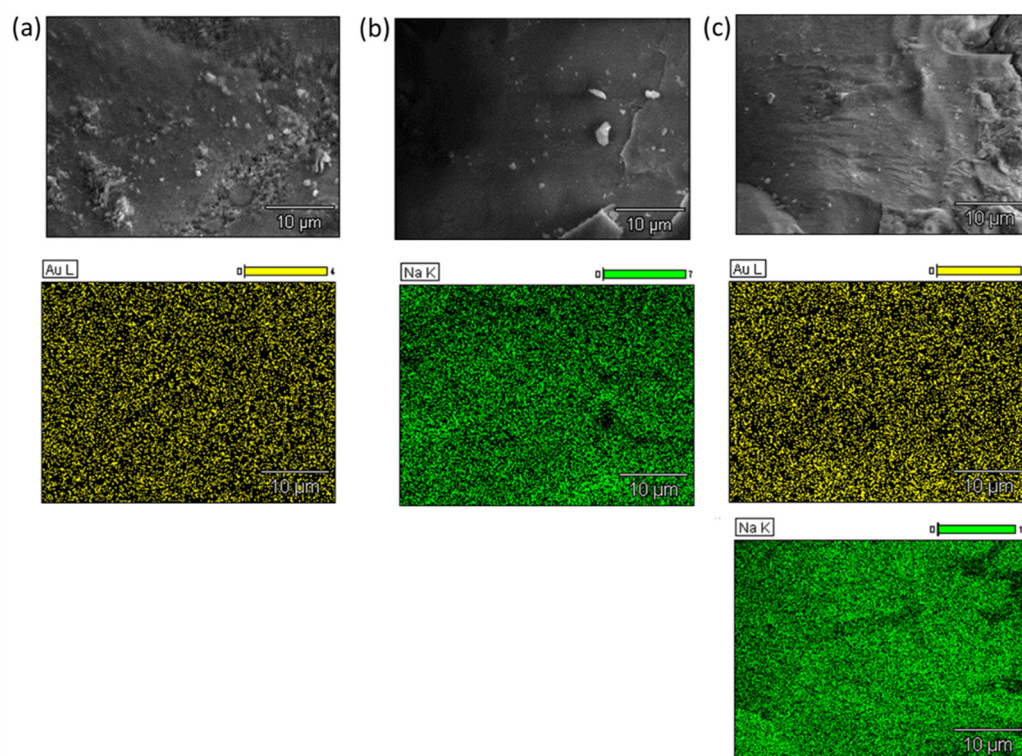
Figure 8. SEM images and corresponding distribution maps (EDX) of Au and Na on the surface of (**a**) Au/CZ, (**b**) Au + 0.3 at% Na/CZ and (**c**) 0.3 at% Na/CZ.
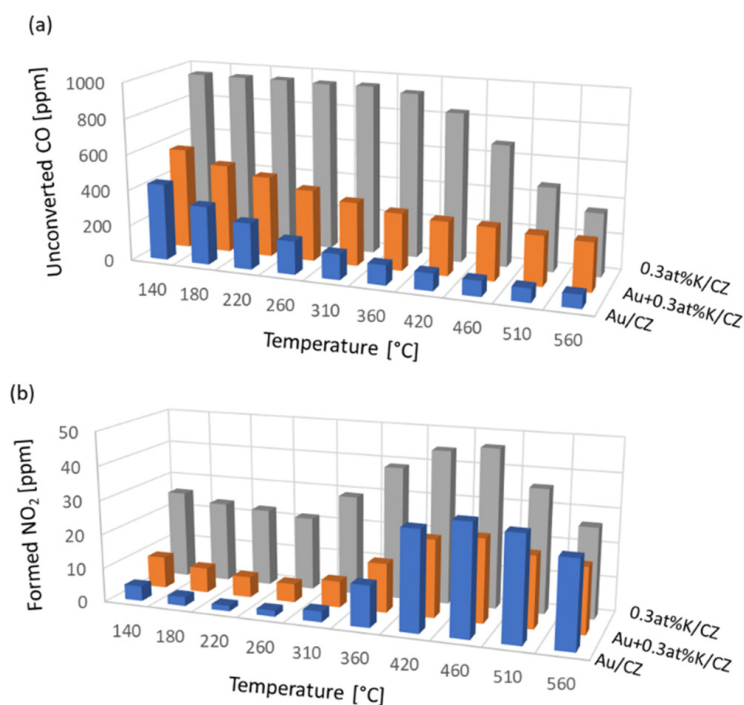

Figure 9. Results from complex stream activity tests: (**a**) CO oxidation and (**b**) NO$_2$ formation.

Because in coal gasification studies lithium has been shown to be the worst catalyst among alkali metal ions and caesium was shown to be better than lithium, sodium, potassium, Li and Cs cations were introduced onto the surface of a preloaded gold catalyst and tested in the model stream. Their loading was 3.0 at% instead of the 0.3 at% applied in the previous tests to verify if the conversion of CO over the alkali-doped catalysts, approaching that of the undoped catalyst due to a low alkali loading or because the effect of the alkali metal ions, becoming negligible at higher temperatures. If the former is true, then for a higher loading, there would most likely be a lower value, which the conversion curves would be approaching. If the latter is true, the effect would probably also become negligible for the higher loading. The CO conversion curves in the model stream, as well as T_{50} values, are displayed in Figure 10. The activity of both the lithium-ion-doped and the caesium-ion-doped gold catalysts approaches the same final value, which is lower than that observed for the undoped gold catalyst.
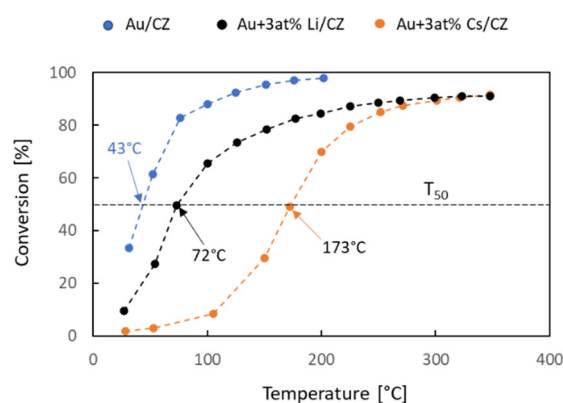

Figure 10. Results of CO oxidation tests in the model stream of Au/CZ, Au + 3 at% Li/CZ and Au3 at% Cs/CZ.

3. Materials and Methods

3.1. Synthesis

Ammonium ceric nitrate (analytical grade, BDH, Randor, PA, USA) was used as the precursor for ceria supports. They were prepared via two routes: (1) thermal decomposition (C_{TD}) and (2) precipitation (C_P). C_{TD} was obtained from the thermal decomposition of the precursor carried out at 550 °C for 4 h. Precipitated ceria was prepared from the same precursor by adding 2.50 dm^3 H$_2$O to 200.0 g of the salt, and a 15% NH$_3$ solution (purum p.a. POCh, Gliwice, Poland) was used as the precipitating agent. The obtained gel was dried at 333 K for 24 h, then at 393 K for another 48 h and was finally calcined at 773 K for 3 h. Commercial ceria (analytical grade, BDH, Randor, PA, USA) was used as a reference. The cerium–zirconium mixed oxide was prepared as described previously [11]. The precipitated ceria and ceria–zirconia were dosed with solutions of Na$_2$CO$_3$ and K$_2$CO$_3$ (both analytical-grade reagents, POCH Gliwice, Gliwice, Poland). Solutions of the carbonates were prepared in 10 mL volumetric flasks with 75 mg and 100 mg of Na$_2$CO$_3$ and K$_2$CO$_3$, respectively. The supports were dosed with 1 mL per 4 g of support.

The gold was deposited from the following precursor: HAuCl$_4$·H$_2$O (analytical grade, Sigma-Aldrich, Oakville, ON, Canada). The catalysts were then calcined at 550 °C for 3 h. Afterwards, the catalyst was divided into nine parts. Four of them were doped with 0.3 at% alkali metal ions, with CO$_3^{2-}$ as the counterion; four of them were doped with 3.0 at% alkali metal ions; and one was used as the reference. Solutions of carbonates of alkali metals for deposition of the lower loading (0.3 at%) were prepared using 0.196 g, 0.283 g, 0.370 g and 0.870 g of M$_2$CO$_3$ for M = Li, Na, K and Cs, respectively (all analytical grade, POCH Gliwice, Gliwice, Poland), dissolved in 100 mL of redistilled water. The catalysts were impregnated with 1 mL of the appropriate solution, and the solvent was evaporated. The catalysts with the higher loading of Na$_2$CO$_3$, K$_2$CO$_3$ and Cs$_2$CO$_3$ were

dosed with 1 mL/g_{cat} of a solution prepared with the same amount of carbonate as for the lower loading dissolved in 10 mL of distilled water. The lower solubility of lithium carbonate did not allow for such a concentration and was therefore prepared using 10 mL of the previously prepared solution. After the deposition and drying of the solvent, the catalysts were calcined at 550 °C for another hour.

3.2. Characterization

The microscope used for SEM imaging was a Quanta FEG 250 (Field Electron and Ion Company, FEI, Hillsboro, OR, USA). Images were recorded with the following parameters: working distance = 10 mm; spot size: 3; beam energy: 10 kV; and magnifications: 5000, 10,000 and 20,000 times. Additionally, the SEM images of the alkali-doped catalysts, i.e., Au + 0.3% alkali ion/CZ, as well as the Au/CZ reference, were acquired with an SEM SU8000 instrument (Hitachi) equipped with a cold field emission gun. The images were obtained at 5 kV, with a working distance of approximately 12 mm and magnifications of 500, 1000, 2000, 5000 and 20,000 times. The EDX maps were recorded with an UltraDry EDS detector (Thermo Scientific) with a resolution of 256 by 192, pixel size: 0.17 um, accelerating voltage of 20 kV at a magnification of 3000 times.

The surface area and pore sizes of samples were obtained by nitrogen physisorption measurements (ASAP 2020, Micromeritics Instrument Corp., Norcross, GA, USA) with approx. 1 g of each sample. First, the samples were degassed for 2 h at 250 °C and then subjected to pulses of nitrogen at the temperature of 77 K; p/p_0 was between 0.01 and 1.0. The Brunauer–Emmett–Teller the BJH model were used for calculations.

X-ray photoelectron spectroscopy (XPS) measurements were performed with a K-Alpha instrument (Thermo Scientific, Waltham, MA, USA). Survey and detailed (C 1s, O 1s, Ce 3d, Au 4f and Zr 3d and alkali metal), number of scans: 5 and 15. Peak fitting was completed using Shirley-type background subtraction and shift to C 1s (285.0 eV). The C 1s-detailed regions were fitted with three peaks located at 285.0 eV, 286.4 eV and 289.1 eV, which correspond to C–C, C–O and COO– groups, respectively. The O 1s regions were fitted with two components, namely the lattice O-O peak at 529.6 eV and the surface hydroxyl group oxygen at 531.4 eV. The Ce 3d regions were fitted with five sets of spin-orbit doublets with a split of 18.4 eV and the following binding energy values of the lower binding energy components: v_0 (880.4 eV), v (882.3 eV), v′ (884.7 eV), v″ (888.7 eV) and v‴ (898.2 eV).

Temperature-programmed reduction (TPR) experiments were carried out with an Autochem 2910 or Autochem 2920 instrument (Micromeritics Instrument Corp., Norcross, GA, USA), each with TCD calibrated for hydrogen consumption. The sample (0.1 g) was first heated to 150 °C (10 °C min^{-1}) in a flow of 5% vol O_2 in an He gas mixture (30 mL min^{-1}). After 10 min at this temperature, the sample was cooled in helium (30 mL·min^{-1}), and the TPR profile was recorded with a ramp of 10 °C/min (30 mL·min^{-1}) with either 5 vol% H_2 in Ar from RT to 1050 °C or 10% H_2/Ar from RT to 900 °C.

A D5000 horizontal goniometer (Bruker AXS GmbH, Karlsruhe, Germany) was used to obtain the XRD patterns with the following parameters: radiation source: Cu (Kα radiation, 1.5418 Å, 40 kV, 40 mA); divergent Bragg–Brentano optics; LynxEye detector; scattering angle range: 20 to 130°. The data were analyzed as in [11]. The average particle size (D) was determined using the Scherrer equation.

Attenuated total reflection Fourier transform infrared spectroscopy (ATR-FTIR) measurements were carried out using a Spectrum Two instrument (Perkin Elmer). For each sample, four scans were collected with a resolution of 4 cm^{-1} within the range of 450 to 4000 cm^{-1}.

Inductively-coupled plasma-optical emission spectroscopy determinations were carried out with an Optima 7000 instrument (Perkin Elmer Inc., Waltham, MA, USA) using approx. 0.3 g of each sample digested and diluted to 100 mL with redistilled water and a subsequent 10-fold dilution. The following parameters were used: pump rate: 1.5 mL/min; 5 external standards; 5 scans/element; radial analysis mode; wavelengths: Au 267.595 nm,

Ce 413.764 nm, Zr 413.727 nm, Li 670.784 nm, K 766.488 nm, Na 589.597 nm and Cs 697.327 nm.

3.3. Activity Measurements

Activity measurements were carried out in a model stream (1 vol% CO + 1 vol% O_2 in He) and a complex stream (1000 ppm CH_4, 150 ppm C_2H_6, 50 ppm C_3H_8, 1000 ppm CO, 200 ppm NO, 7% H_2O, 5% CO_2, 10% O_2, balance N_2). In both cases, the outlet stream composition was determined using infrared spectroscopy. Details of the measurements are given in [11].

4. Conclusions

The influence of the presence of alkali metal ions (Li, Na, K and Cs) on the reducibility of supports and Au catalysts was tested and analyzed in relation to their activity in CO oxidation. The activity of the tested ceria samples substantially varied, and so did their reduction profiles. However, no correlation between their activity and reducibility was observed. The presence of alkali metal ions (Na and K) shifted both reduction peaks of ceria to higher temperatures but did not affect its activity in CO oxidation. The reducibility of the cerium–zirconium mixed oxide proved to be more stable and unaffected by the presence of alkali metal ions (Li, Na, K and Cs). In fact, the T_{max} of the reduction peak was not shifted, even when the potassium ion loading increased from 0.3 at% to 3.0 at%; only the shape changed. In contrast, in the case of the gold catalysts, there was a clear dependence of the CO conversion on the shift of the T_{max} of the first reduction peak. Regardless of the alkali metal ion loading, there was a drop in the activity of the gold catalyst in CO oxidation. At 100 °C, the difference between the activity of the lithium-doped Au/CZ catalyst and the caesium-doped sample was higher than 50%. In a complex stream, the negative effect of the presence of alkali metal ions on the activity of the gold catalysts was also observed in CO oxidation but not for NO oxidation. In the latter, the presence of potassium ions on the activity of Au/CZ showed two temperature regimes; it is beneficial at lower temperatures and detrimental above 350 °C.

References

1. Després, J.; Elsener, M.; Koebel, M.; Kröcher, O.; Schnyder, B.; Wokaun, A. Catalytic oxidation of nitrogen monoxide over Pt/SiO$_2$. *Appl. Catal. B* **2004**, *50*, 73–82. [CrossRef]
2. Hong, Z.; Wang, Z.; Li, X. Catalytic oxidation of nitric oxide (NO) over different catalysts: An overview. *Catal. Sci. Technol.* **2017**, *7*, 3440–3452. [CrossRef]
3. Tang, Y.; Chen, W.; Zhang, H.; Wang, Z.; Teng, D.; Cui, Y.; Feng, Z.; Dai, X. Single-atom metal-modified graphenylene as a high-activity catalyst for CO and NO oxidation. *Phys. Chem. Chem. Phys.* **2020**, *22*, 16224. [CrossRef] [PubMed]
4. Tamai, K.; Hosokawa, S.; Kato, K.; Asakura, H.; Teramura, K.; Tanaka, T. Low-temperature NO oxidation using lattice oxygen in Fe-site substituted SrFeO$_{3-\delta}$. *Phys. Chem. Chem. Phys.* **2020**, *22*, 24181. [CrossRef] [PubMed]
5. Weiman, L.; Haidi, L.; Min, Z.; Yunfa, C. Comparative study of mesoporous Ni$_x$Mn$_{6-x}$Ce$_4$ composite oxides for NO catalytic oxidation. *RSC Adv.* **2019**, *9*, 31035. [CrossRef]
6. Shen, Y.; Ge, X.; Chen, M. Catalytic oxidation of nitric oxide (NO) with carbonaceous materials. *RSC Adv.* **2016**, *6*, 8469–8482. [CrossRef]
7. Zhang, X.; Lin, R. Effect of Alkali Metal Elements on Nitric Oxide Chemisorption at the Edge of Char: A DFT Study. *Energy Procedia* **2019**, *158*, 4805–4809. [CrossRef]
8. Haruta, M. Gold as a low-temperature oxidation catalyst: Factors controlling activity and selectivity. *Stud. Surf. Sci. Catal.* **1997**, *110*, 123–134. [CrossRef]
9. Ramírez Reina, T.; Ivanova, S.; Centeno, M.A.; Odriozola, J.A. Low-temperature CO oxidation on multicomponent gold based catalysts. *Front. Chem.* **2013**, *1*, 12. [CrossRef]
10. Wang, H.-F.; Gong, X.-Q.; Guo, Y.-L.; Guo, Y.; Lu, G.; Hu, P. Structure and Catalytic Activity of Gold in Low-Temperature CO Oxidation. *J. Phys. Chem. C* **2009**, *113*, 6124–6131. [CrossRef]
11. Iwanek, E.; Liotta, L.F.; Williams, S.; Hu, L.; Calilung, L.F.; Pantaleo, G.; Kaszkur, Z.; Kirk, D.W.; Gliński, M. Application of Potassium Ion Deposition in Determining the Impact of Support Reducibility on Catalytic Activity of Au/Ceria-Zirconia Catalysts in CO Oxidation, NO Oxidation, and C$_3$H$_8$ Combustion. *Catalysts* **2020**, *10*, 688. [CrossRef]
12. Kim, H.J.; Jang, M.G.; Shin, D.; Han, J.W. Design of Ceria Catalysts for Low-Temperature CO Oxidation. *ChemCatChem* **2019**, *12*, 11–26. [CrossRef]
13. Wu, C.; Guo, Z.; Chen, X.; Liu, H. Cu/CeO$_2$ as efficient low-temperature CO oxidation catalysts: Effects of morphological structure and Cu content. *React. Kinet. Mech. Catal.* **2020**, *131*, 691–706. [CrossRef]
14. Kung, H.H.; Kung, M.C.; Costello, C.K. Supported Au catalysts for low temperature CO oxidation. *J. Catal.* **2003**, *216*, 425–432. [CrossRef]
15. Gulyaev, R.V.; Slavinskaya, E.M.; Novopashin, S.A.; Smovzh, D.V.; Zaikovskii, A.V.; Osadchii, D.Y.; Bulavchenko, O.A.; Korenev, S.V.; Boronin, A.I. Highly active PdCeO$_x$ composite catalysts for low-temperature CO oxidation, prepared by plasma-arc synthesis. *Appl. Catal. B Environ.* **2014**, *147*, 132–143. [CrossRef]
16. Sudarsanam, P.; Mallesham, B.; Reddy, P.S.; Großmann, D.; Grünert, W.; Reddy, B.M. Nano-Au/CeO$_2$ catalysts for CO oxidation: Influence of dopants (Fe, La and Zr) on the physicochemical properties and catalytic activity. *Appl. Catal. B Environ.* **2014**, *144*, 900–908. [CrossRef]
17. Kim, I.H.; Seo, H.O.; Park, E.J.; Han, S.W.; Kim, Y.D. Low Temperature CO oxidation over Iron Oxide Nanoparticles Decorating Internal Structures of a Mesoporous Alumina. *Sci. Rep.* **2017**, *7*, 40497. [CrossRef]
18. Dey, S.; Dhal, G.C.; Mohan, D.; Prasad, R. Synthesis of highly active Cobalt catalysts for low temperature CO oxidation. *Chem. Data Coll.* **2019**, *24*, 100283. [CrossRef]
19. Iwanek, E.M.; Liotta, L.F.; Williams, S.; Hu, L.; Ju, H.; Pantaleo, G.; Thapar, A.; Kaszkur, Z.; Kirk, D.W.; Gliński, M. Activity of Ag/CeZrO$_2$, Ag+K/CeZrO$_2$, and Ag-Au+K/CeZrO$_2$ Systems for Lean Burn Exhaust Clean-Up. *Catalysts* **2021**, *11*, 1041. [CrossRef]
20. Gonzalez, E.; Rangel, R.; Solís-Garcia, A.; Venezia, A.M.; Zepeda, T.A. FTIR investigation under reaction conditions during CO oxidation over Ru$_{(x)}$-CeO$_2$ catalysts. *Mol. Catal.* **2020**, *493*, 111086. [CrossRef]
21. Li, Q.; Wang, X.; Xin, Y.; Zhang, Z.; Zhang, Y.; Hao, C.; Meng, M.; Zheng, L.; Zheng, L. A unified intermediate and mechanism for soot combustion on potassium supported oxides. *Sci. Rep.* **2014**, *4*, 4725. [CrossRef] [PubMed]
22. Aneggi, E.; de Leitenburg, C.; Dolcetti, G.; Trovarelli, A. Diesel soot combustion activity of ceria promoted with alkali metals. *Catal. Today* **2008**, *136*, 3–10. [CrossRef]
23. Castoldi, L.; Matarrese, R.; Lietti, L.; Forzatti, P. Intrinsic reactivity of alkaline and alkaline-earth metal oxide catalysts for oxidation of soot. *Appl. Catal. B Environ.* **2009**, *90*, 278–285. [CrossRef]
24. Jakubek, T.; Hudy, C.; Stelmachowski, P.; Nowicka, E.; Golunski, S.; Kotarba, A. Influence of Different Birnessite Interlayer Alkali Cations on Catalytic Oxidation of Soot and Light Hydrocarbons. *Catalysts* **2020**, *10*, 507. [CrossRef]
25. Azancot, L.; Bobadilla, L.F.; Centeno José, M.A.; Odriozola, A. IR spectroscopic insights into the coking-resistance effect of potassium on nickel-based catalyst during dry reforming of methane. *Appl. Catal. B Environ.* **2021**, *285*, 119822. [CrossRef]
26. Osaki, T.; Mori, T. Role of potassium in carbon-free CO$_2$ reforming of methane on K promoted Ni/Al$_2$O$_3$ catalysts. *J. Catal.* **2001**, *204*, 89–97. [CrossRef]
27. Giordano, F.; Trovarelli, A.; Leitenburg, C.; Giona, M. A Model for the Temperature-Programmed Reduction of Low and High Surface Area Ceria. *J. Catal.* **2000**, *193*, 273–282. [CrossRef]

28. Venezia, A.M.; Pantaleo, G.; Longo, A.; Di Carlo, G.; Casaletto, M.P.; Liotta, L.F.; Deganello, G. Relationship between Structure and CO Oxidation Activity of Ceria-Supported Gold Catalysts. *J. Phys. Chem. B* **2005**, *109*, 2821–2827. [CrossRef]

29. Tang, W.; Weng, J.; Lu, X.; Wen, L.; Suburamanian, A.; Nam, C.-Y.; Gao, P.-X. Alkali-Metal Poisoning Effect of Total CO and Propane Oxidation over Co_3O_4 Nanocatalysts. *Appl. Catal. B Environ.* **2019**, *256*, 117859. [CrossRef]

30. Spiro, C.L.; McKee, D.W.; Kosky, P.G.; Lamby, E.J.; Maylotte, D.H. Significant parameters in the catalysed CO_2 gasification of coal chars. *Fuel* **1983**, *62*, 323–330. [CrossRef]

31. Salavati-fard, T.; Lobo, R.F.; Grabow, L.C. Linking low and high temperature NO oxidation mechanisms over Brønsted acidic chabazite to dynamic changes of the active site. *J. Catal.* **2020**, *389*, 195–206. [CrossRef]